MA-class linear transformer driver for *Z*-pinch research

F. Conti,[*] J. C. Valenzuela,[†] V. Fadeev, N. Aybar, D. B. Reisman, A. Williams, G. Collins IV, J. Narkis, M. P. Ross,[‡] and F. N. Beg

Center for Energy Research, University of California San Diego, La Jolla, California 92093, USA

R. B. Spielman

Laboratory for Laser Energetics, University of Rochester, Rochester, New York 14623, USA and Idaho Accelerator Center, Idaho State University, Pocatello, Idaho 83201, USA

(Received 17 April 2020; accepted 17 August 2020; published 28 September 2020)

A linear transformer driver (LTD) generator capable of delivering up to 0.9 MA current pulses with 160 ns rise time has been assembled and commissioned at University of California San Diego. The machine is an upgrade of the LTD-III pulser from Sandia National Laboratories, consisting of 40 capacitors and 20 spark gap switches, arranged in a 20-brick configuration. The driver was modified with the addition of a new trigger system, active premagnetization of the inductive cores, a vacuum chamber with multiple diagnostic ports, and a vacuum power feed to couple the driver to plasma loads. The new machine is called compact experimental system for *Z*-pinch and ablation research (CESZAR). The driver has a maximum bipolar charge voltage of ± 100 kV, but for reliability and testing, and to reduce the risk of damage to components, the machine was operated at ± 60 kV, producing 550 kA peak currents with a rise time of 170 ns on a 3.5 nH short circuit. While the peak current is scaled down due to the reduced charge voltage, the pulse shape and circuit parameters are close to the results of the cavity and power feed models but suggest a slightly higher inductance than predicted. The machine was then used to drive wire array *Z*-pinch and gas puff *Z*-pinch experiments as initial dynamic plasma loads. The evolution of the wire array *Z* pinch is consistent with the general knowledge of this kind of experiment, featuring wire ablation and stagnation of the precursor plasma on axis. The gas puff *Z* pinches were configured as a single, hollow argon gas shell, in preparation for more structured gas puff targets such as multispecies, multishell implosions. The implosion dynamics agree generally with 1D magnetohydrodynamics simulation results, but large zippering and magneto-Rayleigh-Taylor instabilities are observed. The CESZAR load region was designed to accommodate many load types to be driven by the machine, which makes it a versatile platform for studying *Z*-pinch plasmas. The completion of the CESZAR driver allows plasma experiments on energy coupling from LTD machines to plasma loads, instability mitigation techniques and magnetic field distributions in *Z* pinches, and interface dynamics in multispecies implosions.

DOI: 10.1103/PhysRevAccelBeams.23.090401

I. INTRODUCTION

Linear transformer drivers (LTDs) are a promising pulse generator configuration, as they do not require pulse-forming lines like conventional systems based on Marx bank technology to produce short (100–300 ns) pulses [1,2]. This provides potential advantages, including a smaller footprint, higher energy efficiency, low intrinsic impedance, and modular design [3–6].

The LTD concept was pioneered by Koval'chuk *et al.* [7] and has received increasing attention in recent years [8–11], including a recent review on the history of LTD development [12]. Several LTD machines are operational or under development in the USA [13–16], Europe [17,18], Russia [19,20], and Asia [21,22].

LTDs are induction generators where a voltage is produced across an insulator gap on the inside of an induction cavity, which contains several high-energy-density capacitors and high-voltage switches packaged compactly as "bricks". The bricks are arranged in parallel inside the inductive metal housing.

In air-insulated LTD cavities, bricks are usually made of one capacitor and one switch. A machine with this design,

[*]fconti@ucsd.edu
[†]Present address: Instituto de Fisica, Pontificia Universidad Catolica de Chile, Santiago, Chile.
[‡]Present address: Naval Information Warfare Center Pacific, San Diego, California 92152, USA.

consisting of 12 capacitors in parallel, is the GenASIS driver already present at University of California (UC) San Diego [14]. While air insulation makes these cavities easy to service, it also limits their compactness and maximum power. Oil-insulated cavities can sustain a higher charge voltage in a smaller space, so they are often configured with two capacitors in series per brick (charged at opposite polarities to effectively double the operating voltage) and a large number of bricks (20–40) arranged in a toroidal-shaped cavity. The LTD described here is of the second type.

The use of many bricks in parallel results in a circuit with low inductance, suitable for producing fast, high-current electrical pulses. Multiple layers of bricks ("stages") can be connected in series inside the same cavity to increase the output voltage, and multiple cavities can be connected in parallel to increase the output current. Therefore, LTD stages can potentially be used as building blocks for larger, modular machines.

A transmission line or power feed occupies the inner part of the cavity to couple the electrical pulse from the capacitors to the load [9]. Ferromagnetic cores can be placed inside the cavity to prevent current from taking a parasitic current path around the cavity enclosure. This parasitic current path is electrically in parallel with the path that includes the power feed and load. The ferromagnetic cores inductively isolate this parasitic current path from the power feed and load.

The machine described in this work is based on the LTD-III cavity received from Sandia National Laboratories, where it was extensively tested with resistive loads, but it was not configured with a power feed to drive plasma loads [23]. The machine was modified with a new trigger system, an active premagnetization circuit for the ferromagnetic cores, a vacuum chamber for diagnostic access, and a vacuum power feed to propagate the current pulse to the load. The newly upgraded LTD is called compact experimental system for *Z*-pinch and ablation research (CESZAR) and is a flexible pulsed power driver for plasma experiments.

The completion of the CESZAR generator allows experiments to be conducted on a variety of topics relevant to high-energy density (HED) science, such as the energy coupling between a low-impedance LTD and plasma loads, interface dynamics of multishell, multispecies implosions, and dynamics of magnetized *Z* pinches. The driver will also provide an excellent platform for developing advanced diagnostic techniques such as spectroscopic measurements of magnetic fields in HED plasmas.

This paper is organized as follows. In Sec. II, a description of the CESZAR machine is presented. In Sec. III, results from circuit modeling and machine testing are reported. In Sec. IV, results from two plasma load configurations are presented. In Sec. V, we summarize our work and provide some concluding remarks.

II. THE CESZAR MACHINE

The CESZAR machine is comprised of two main sections: the LTD cavity enclosure and the vacuum chamber. The main subsystems that comprise each section will be described below.

The LTD cavity is enclosed by a 2-m-diameter, 0.2-m-tall circular metal housing and contains the LTD bricks, a trigger line relayed to all the bricks, two ferromagnetic cores, plastic insulators, and connections for compressed air and machine diagnostics. The cavity is filled with transformer oil (Shell Diala S2-ZX-A) for electrical insulation, with particular care paid to ensure a minimal amount of air bubbles remain in the cavity. Each brick in the cavity is composed of two 58 nF, 100 kV capacitors (General Atomics 35464) connected in series by one triggered spark gap switch (L-3 Communications, Pulse Sciences Division, part no. 40264-200SD [24]).

During the charging phase, the top row of capacitors is charged to a negative voltage $-V_c$ while the bottom row of capacitors is charged to the opposite voltage $+V_c$ (V_c can be adjusted between 40 and 100 kV). The charging resistors are of the epoxy-coated ceramic composite type, with a 250 kΩ resistance at the output of the charging power

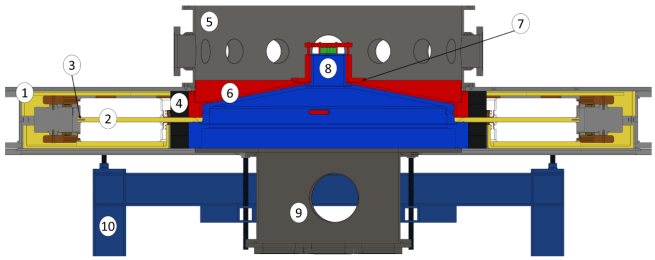

(a)

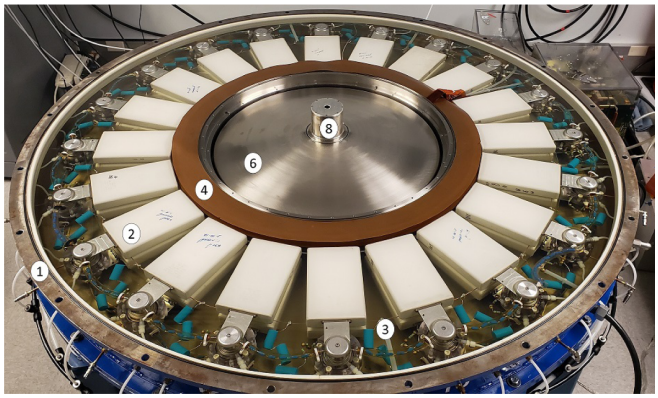

(b)

FIG. 1. (a) Cross-section CAD drawing of the LTD machine, with highlighted relevant components. 1 = LTD cavity, 2 = LTD bricks, 3 = trigger line, 4 = ferromagnetic cores, 5 = vacuum chamber, 6 = vacuum power feed, 7 = location of B-dot probes, 8 = load region, 9 = vacuum pumps spool, and 10 = support frame. (b) Photo of the LTD cavity without the vacuum chamber, power feed anode, and cavity lid.

supply and 108 kΩ between adjacent bricks for each polarity. A total voltage difference of $2V_c$ is present across each switch when the charge is complete, and the voltage propagates to the output in the vacuum section after the switches are closed.

The vacuum section is comprised of the target chamber, a low-inductance vacuum power feed line, and the load region that allows the machine pulse to be coupled to various plasma loads.

A cross-section computer-aided design (CAD) drawing of the machine is shown in Fig. 1(a), with numbers to highlight the major components including the LTD cavity enclosure, the LTD bricks, the trigger line, the ferromagnetic cores, the vacuum chamber, the vacuum feed with the location of B-dot probes, the load region, the vacuum pumping connections, and the support frame. A photograph of the LTD machine is shown in Fig. 1(b), where the vacuum chamber was removed and the cavity was opened.

The remainder of this section will describe more in detail some key components of the cavity enclosure (trigger circuit and core premagnetization system) and the vacuum assembly (vacuum chamber and power feed).

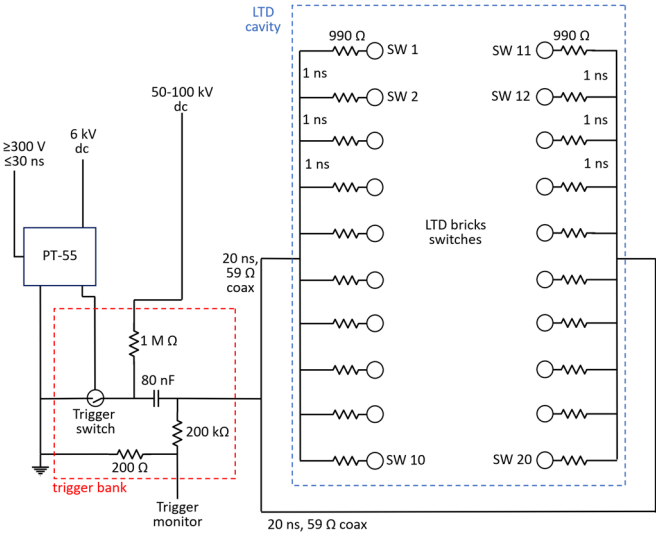

FIG. 2. Schematic of the CESZAR trigger circuit. An 80-nF capacitor bank is used to trigger the 20 switches inside the LTD cavity, with resistive coupling between the bricks. The dashed lines enclose the main units (trigger bank and LTD cavity). The 20 ns, 59 Ω cable length is present in both branches of the trigger line outside the cavity.

A. Trigger circuit

The trigger circuit is a fundamental component of LTD generators, since accurate control (and monitoring) of the closing time for each switch in an LTD is essential to deliver the desired current pulse to the load [25]. For example, triggering the switches in a predetermined sequence allows tailoring of the current pulse [26], while, in order to have the fastest rise time and maximum peak current from a single LTD cavity, the switches should fire simultaneously [27]. The switches used in the CESZAR LTD have two 6.4 mm gaps symmetric around a trigger midplane. The electrodes are charged at opposite polarities, while the midplane is held weakly at ground potential during the charging cycle. The switches operate with ultrazero-type air (≤2 ppm water content) at a pressure of up to 10 bar for a charging voltage up to ±100 kV. It is worth noting that, in order to achieve reliable operation and reduce the prefire occurrence rate to ∼1%, the operating voltage had to be set at 60% of the self-breakdown voltage instead of the 70% reported in the literature for this type of switch [24]. This translates to a 20%–30% higher operational pressure for any given voltage. The higher pressure needed to prevent prefires was more evident when the full cavity was tested with 20 bricks, while the required pressure was closer to the reported curve when testing individual switches. We are still investigating the source of this discrepancy.

A schematic of the trigger circuit for the bricks inside CESZAR is shown in Fig. 2. A solid-state pulse generator, producing a 300 V pulse with 20 ns rise time, is used to trigger a PT-55 high-voltage pulse generator (50 kV, 2 ns rise time). This high-voltage pulse is used to trigger a single spark gap switch (trigger switch) connected to an 80-nF capacitor bank rated for 100 kV charge voltage (trigger capacitor). The trigger capacitor produces a negative-polarity pulse for the trigger plane in the cavity switches. The charge voltage of the trigger capacitor bank is equal to or higher than the single-polarity charge voltage of the LTD capacitors in the cavity: for example, for a cavity charge voltage $V_c = \pm 50$ kV, the recommended trigger voltage is $V_t \geq 50$ kV.

The output pulse is monitored by a resistive voltage divider, and it is split into two 59 Ω high-voltage cables with a propagation time of 20 ns (Dielectric Sciences item no. 2121). Each cable enters the cavity and connects to the middle of a trigger wire aligned around the cavity in a groove at the outer edge of the midplane insulator [see Fig. 1(a)]. Each trigger line connects to ten bricks, five on each side of the cable entering the cavity. The signal propagation delay between two consecutive bricks is 1 ns, and the four-branch trigger line allows for a maximum propagation delay of 5 ns between any two bricks. Each switch connects to the trigger line via a 990 Ω resistor (3x HVR APC C2654A331L, 330 Ω epoxy-coated ceramic composite resistors in series) to provide insulation between bricks on a timescale of ≳10 ns, which is necessary for reliable parallel operation [16].

Each of the 20 switches is monitored by a capacitive voltage probe sensitive to the time derivative of the electric field near the switch midplane (D dot). Even without being calibrated for signal amplitude, the switch monitor probes provide information about the closing time of the LTD bricks.

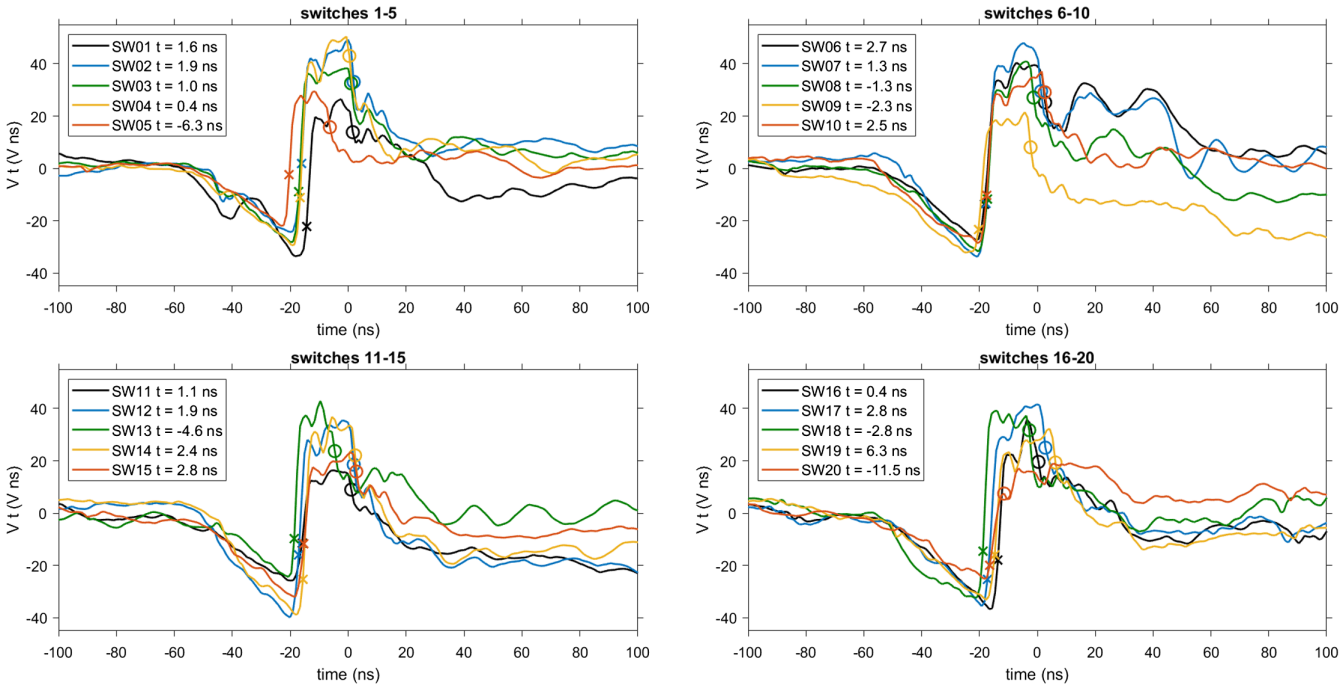

FIG. 3. Example of time-integrated switch monitor signals for the 20 bricks inside the CESZAR cavity. The cross marks identify the local maxima of the nonintegrated signals, while the circles indicate local minima corresponding to the switch closure. The timescale is relative to the average closing time of the 20 switches.

An example of time-integrated D-dot signals is shown in Fig. 3. The initial negative pulse with a rise time of 30 ns represents the charging of the switch midplane to the negative trigger voltage. The gap between the trigger plane and positively charged electrode closes first, resulting in a rapid increase of the midplane voltage. This is indicated by cross marks in the figure, corresponding to the local maxima of the D-dot signal. After a short time, the gap between the two main electrodes in the switch closes, and the midplane voltage floats closer to the ground potential. The closing time of the main gap (local D-dot minima indicated by circles) relative to the average of the 20 bricks is labeled in the legend and ranges from -11.5 to $+6.3$ ns, with a standard deviation of 3.9 ns. This indicates good synchronization of the bricks, which is essential to obtain the maximum peak current in the load.

B. Core premagnetization circuit

Two ferromagnetic cores, one for each polarity, are located at the output of the LTD bricks in order to provide inductive isolation of the vacuum power feed and reduce parasitic current losses around the cavity body. When the switches are triggered, the current path around the cavity enclosure is suppressed by the high-inductance magnetic cores until they saturate. Each core consists of two Metglas® alloy 2605CO toroids, each made of 23-μm-thick and 3.6-cm-tall metallic glass tape wound around a supporting ring with an 86-cm diameter, with insulator between adjacent layers of ferromagnetic material. Each 2605CO alloy toroid has a saturation magnetic induction $B_{\mathrm{sat}} = 1.7$ T and a saturation magnetic field intensity $H_{\mathrm{sat}} = 3$ A/m. Premagnetization of the cores with an initial $-B_0$ (opposite to the field produced by the LTD current) extends the available magnetic field before the cores saturate.

A pulsed premagnetizing circuit is used on the CESZAR machine. A 200 μF capacitor bank is charged to 4 kV and discharged by a triggered spark gap. The pulse is split in two branches: Each branch is composed of a solenoid ($L = 80$ μH), a feedthrough to enter the cavity, and a single loop around one core (two toroids). The loop is insulated with four layers of 125-μm-thick Kapton foil.

The resulting premagnetizing pulse has a rise time of 140 μs and a peak total current of 6 kA, which is more than enough to saturate the four toroids. The premagnetizing current pulse is timed so that its peak occurs at the time of the LTD cavity trigger ("active" premagnetization [2]). The premagnetization has been observed to increase the output peak current of the generator during short-circuit tests, as discussed briefly in Sec. III.

C. Vacuum chamber and diagnostic access

The target vacuum chamber has an inner diameter of 82 cm and is 25 cm tall, which provides room to install compact diagnostics directly inside the chamber. A total of 16 vacuum flanges located around the chamber circumference are for diagnostic access with a radial (equatorial) line of sight to the load, and two viewports are located

vertically above and below the machine on an axial (polar) line of sight. The flanges are DN75 or DN100 standard Conflat type, with a 7.5 or 10 cm bore diameter, respectively, which allows a maximum collection angle of 12°, or 3×10^{-2} sr solid angle. The equatorial viewports are vertically centered around the load.

The vacuum pumping system is comprised of two turbomolecular pumps and a dry roughing pump, and it connects to a secondary section of the vacuum chamber under the cavity [see Fig. 1(a)]. The vacuum system can reach a pressure of 5×10^{-5} mbar or lower in ∼1 h, depending on the load configuration and installed diagnostics.

The core diagnostics presently installed on the machine include time-integrated and time-gated imaging, x-ray photodetectors, and laser probing. These instruments will be described in Sec. IV.

D. Vacuum power feed

The purpose of the radial vacuum feed is to deliver the energy stored inside the cavity to low-impedance loads as efficiently as possible. To maximize the energy coupled to the load, the inductance of the transmission line should be as low as practically possible, since the peak current produced by a driver is inversely proportional to the square root of the circuit inductance. The design of a power feed is usually a trade-off between the need to keep the inductance low, the need to keep the electrical field below the electrical breakdown threshold, and accessibility requirements for diagnostics. This is especially true for low-inductance drivers like single-cavity LTDs.

From the capacitors' output connections on the inner side of the oil-filled cavity, the electrical pulse must propagate radially inward to the machine axis and vertically upward to allow diagnostic access. A curved, dome-shaped transmission line would provide the least possible induction for this kind of path [28]. However, given that a conical power feed is not far from the optimal inductance and is much simpler in design and fabrication, it still represents a good solution for small- and medium-scale laboratory environments [29].

The CESZAR vacuum power feed, shown in Fig. 4, is based on a design calculated for Sandia National Laboratories [30]. Starting from the oil-vacuum interface at the output of the capacitors, a transmission line consisting of an outer coaxial section (of outer radius 39.5 cm), a tapered conical section, and an inner coaxial section (of outer radius 6 cm) was adopted. This geometry allows a considerable fraction of the vertical translation to be located at a large radius (reducing inductance) and limits the amount of plasma-emitted radiation that can reach the insulator at the beginning of the feed. The tapered cone angle of approximately 11° was chosen to raise the load enough to allow equatorial diagnostic access. The upper conical electrode (the anode) has a flat top to allow mounting of diagnostic components inside the vacuum

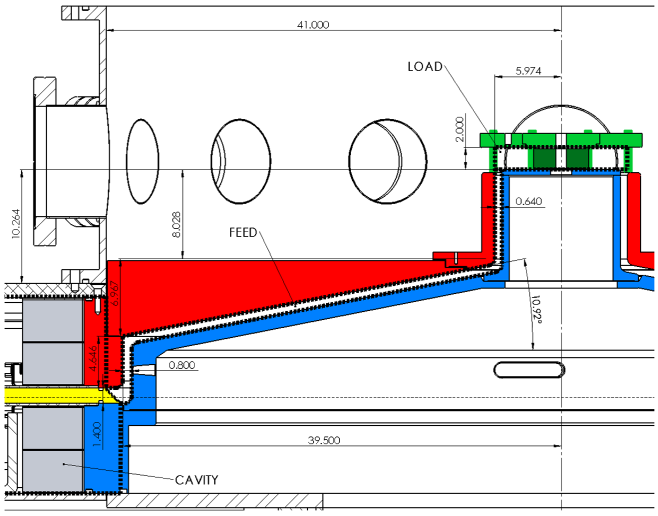

FIG. 4. Cross-section drawing of the vacuum power feed. All dimensions are in centimeters. The anode electrode is colored in red, the cathode electrode is colored in blue, the cavity insulating plate is colored in yellow, and a short-circuit example load is colored in green. The dashed lines delimit the cavity on the left, the vacuum feed in the middle, and the load regions near the axis.

chamber, while the lower electrode (the cathode) has four cut-out slots to allow vacuum pumping from the bottom end of the chamber; one of these slots can be seen directly under the load region in Fig. 4. The dimensions of the inner coaxial section were chosen in order to be able to install a gas injector with a diameter up to 8 cm.

The vacuum gap between the electrodes decreases from an initial value of 0.8 cm to a final value of 0.64 cm along the conical section of the power feed. Calculations of the electric field distribution in the feed conducted with the SCREAMER code [31,32] with a charge voltage $V_c = \pm 100$ kV and a load inductance of 8 nH (a realistic value for most gas loads and some wire loads) show that the electric field does not exceed 150 kV/cm anywhere in the feed, which is well below the electron emission threshold of 200 kV/cm used for most electrode materials [33]. The dashed lines in Fig. 4 delimit the cavity (on the left side), the vacuum feed gap region (delimited by the electrodes in red and blue), and the load region near the axis (green components).

The material chosen for the transmission line electrodes was 304 stainless steel, due to its high strength, low cost, and relatively high resistivity compared to other metals. A higher-resistivity material can introduce small resistive losses, slightly increasing the damping of the circuit and reducing oscillations of low-loss systems. Large oscillations are potentially dangerous for several components in high-power systems, particularly the energy storage capacitors that are not typically designed for rapid voltage reversals.

The vacuum feed inductance was calculated to be 5.2 nH prior to fabrication of the vacuum feed, using the magnetic

field distribution from calculations done with the COMSOL Multiphysics® software. The domains for the calculation are delimited by the dashed lines in Fig. 4 and marked as "feed" and "load."

III. CIRCUIT MODEL AND MACHINE SHORT-CIRCUIT TESTS

The CESZAR driver circuit was modeled with the COMSOL software and the SCREAMER circuit analysis code. Developing an equivalent circuit model requires appropriate calculations of the relevant impedances.

The series inductance of each brick can be calculated as approximately 172 nH [23], so the inductance of the 20-brick parallel arrangement should be about 8.6 nH. However, the cavity inductance measured in Ref. [23] using smaller 40 nF capacitors was 0.8 nH higher than the calculated value. The inductance of the cavity alone was not measured with the current 58 nF capacitors, but it is reasonable to expect a similar increase to ~9 nH in the cavity inductance. The expected series resistance of each brick is about 300 mΩ, or 15 mΩ for the cavity.

As mentioned above, the vacuum feed inductance was calculated to be 5.2 nH, and its series resistance was calculated to be 3 mΩ. The design value for the total driver inductance is therefore $L_D = 14.2$ nH. The magnetic cores were modeled as a shunt resistance (defined simply as the load voltage divided by the loss current around the cavity body) with a value of 1.9 Ω [23].

After the initial assembly, the machine was tested with a short-circuit load in order to measure the driver inductance. The load was a 25-mm-radius, 20-mm-long aluminum cylinder: with the return current radius $R_r = 6$ cm, it results in a load inductance $L_{short} = 3.5$ nH and an expected total circuit inductance $L_D + L_{short} = 17.7$ nH.

To reduce the stress on the LTD components in such a low-loss configuration, particularly to limit the voltage reversal that is applied to the capacitors during *LC* oscillations, and to test the system reliability, the machine was charged to $V_c = \pm 60$ kV, which is below the maximum rating of ±100 kV.

The current was measured with a set of three differential B-dot probes arranged circularly at the base of the inner coaxial section of the vacuum feed [see Fig. 1(a)]. Each B-dot probe consists of two individual, single-loop coils wound in opposite directions. The probes were calibrated *in situ* against a 5 mΩ current-viewing resistor (T&M Research Products model K-1000-2). The total circuit inductance can be calculated by fitting an *RLC* waveform to the measured current pulse, and then the driver inductance can be obtained by simply subtracting the load inductance from the circuit inductance.

An example of a test shot with the 3.5 nH short-circuit load, conducted with a charge voltage $V_c = \pm 60$ kV, is shown in Fig. 5. The measured peak current is 552 kA, and the time to peak is 173 ns. We note here that, even at reduced charge voltage, core premagnetization plays an important effect in the output current: Without premagnetization, the measured peak current decreased from 550 to 350–400 kA, probably due to a higher shunt current around the cavity body.

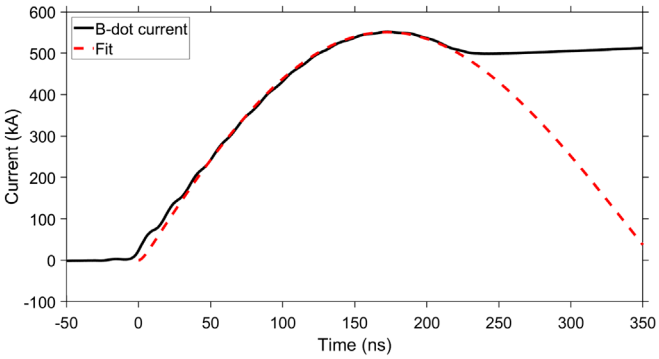

FIG. 5. Example of a current pulse with a 3.5 nH short-circuit load, for a charge voltage $V_c = \pm 60$ kV. The dashed line is a least-squares fit to an *RLC* pulse with $L = 22$ nH and $R = 21$ mΩ.

The least-squares fit to an *RLC* series circuit current pulse for times $t \leq 220$ ns results in a measured inductance $L_M = 22 \pm 1$ nH and $R_M = 21 \pm 6$ mΩ. Subtracting the load inductance, the corresponding driver inductance is 18.5 nH, which is 30% higher than the expected value of 14.2 nH. The set of connections used in the LTD bricks, modified from LTD-III connections [23], could be responsible for at least a portion of the increased cavity inductance. Another possible explanation to the increased apparent inductance could be a nonsynchronous closing of the 20 switches in the cavity. The switch monitor signals indicate that this should not be the case, but the scenario was explored nevertheless with the SCREAMER code using the circuit model in Fig. 6. We have not been able to reproduce the rise time, peak current, and sinusoidal profile of the measured current simply by changing the closing time of the switches in the model. We are still investigating possible sources of the extra measured inductance.

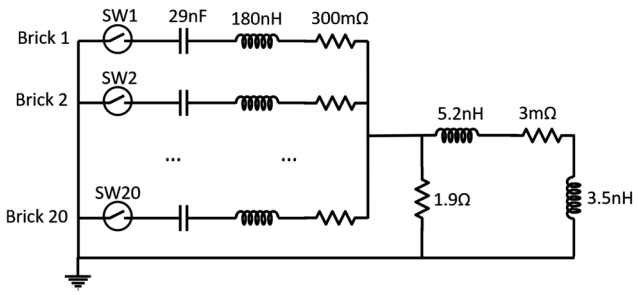

FIG. 6. Circuit model of the CESZAR machine with the 20 bricks in parallel, the magnetic cores modeled as 1.9 Ω shunt resistance, the power feed modeled as a 5.2 nH inductance, 3 mΩ resistance, and a 3.5 nH short-circuit load.

TABLE I. Comparison of nominal design parameters for the CESZAR machine with capacitors charged to ±100 and ±60 kV and results of the 3.5 nH short-circuit tests with capacitors charged to ±60 kV.

	Model (100 kV)	Model (60 kV)	Test (60 kV)
Number of bricks		20	
Number of capacitors		40	
Capacitor size		58 nF	
Charge voltage	±100 kV	±60 kV	±60 kV
Stored energy	11.6 kJ	4.2 kJ	4.2 kJ
Driver inductance	14.2 nH	14.2 nH	18.5 nH
Driver impedance	0.16 Ω	0.16 Ω	0.18 Ω
Peak current (3.5 nH short circuit)	0.98 MA	0.59 MA	0.55 MA

The discrepancy between measured and model current waveforms at later times ($t \geq 220$ ns), when the B-dot current trace becomes nearly flat instead of following the LC oscillation, is likely due to the formation of plasma in the vacuum feed. Plasma in the feed region could shunt the driver current upstream of the B-dot location (for example, as a result of flashover at the surface of the vacuum insulator), or it could surround the probe [29]. In both cases, the magnetic flux change seen by the probe would be greatly reduced. After the current peak, the energy flux and $E \times B$ drift velocity reverse direction and point outward (power reversal) [9,29], which can cause plasma to be emitted by the feed electrodes via the inverse skin effect and propagate upstream toward larger radii. This phenomenon is not expected to affect experiments on the CESZAR driver, which will largely be limited to a timescale ≤220 ns, in order to achieve high-energy coupling given the machine rise time.

Table I summarizes the nominal design specifications for the CESZAR driver, compared to the results of the 3.5 nH short-circuit tests at $V_c = \pm 60$ kV charge voltage. The maximum current measured in the test is close to the 0.59 MA of the model with the same charge voltage. If we assume a linear scaling of the test current pulse up to the maximum charge voltage of 100 kV, we obtain a current of 0.92 MA, which is near the design value.

The driver impedance, calculated as $\sqrt{L/C}$, is approximately 0.18 Ω, which is approximately 10% of the 1.9 Ω shunt resistance reported for the cores, indicating that the current loss around the cavity body should be a small but non-negligible fraction even in the short-circuit configuration. Higher impedance loads, such as imploding Z pinches, could result in a larger fraction of current loss.

IV. EXPERIMENTS WITH PLASMA LOADS

The load region of the CESZAR machine was designed to accommodate various load configurations, which makes it a versatile platform for studying HED plasmas. Some load configurations that can be readily installed on the machine are gas puff Z pinches, wire array Z pinches, and X pinches. Two sets of initial plasma experiments, namely, wire array Z pinches and gas puff Z pinches, are discussed in the remainder of this section. These initial experiments were conducted with a charge voltage $V_c = \pm 50$–60 kV, with resulting peak currents around 400 kA, depending on the load impedance. The operating charge voltage will be increased for future experiments requiring higher current levels.

A. Wire array Z pinch

The first plasma loads driven on CESZAR were wire array Z pinches. Since first introduced over 40 years ago [34], wire array Z pinches have been studied as a powerful source of x rays [35–37]. Two advantages of wire arrays are that the initial load mass distribution is well defined and that it can be adjusted easily by changing the number and material of the wires.

The overall behavior of a wire array Z pinch occurs in phases [38]. First, the outer wire material is vaporized, and plasma forms and expands from each wire. The majority of the wire mass remains in the dense cold wire cores, surrounded by a low-density hot coronal plasma that carries the driver current. The $\mathbf{J} \times \mathbf{B}$ force acts on the coronal plasma that is continuously ejected with an ablation velocity $v_a \sim 100$ km/s [39,40]. There is a pronounced difference between arrays with few wires and large interwire gaps, where the precursor plasma flows inward in streams, and arrays with many wires and small interwire gaps, where the array behaves more like a single shell [41], producing a much higher x-ray power [42].

Initially, a coronal plasma surrounded by a "local" magnetic field with closed field lines forms around the wire cores. The coronal plasma is subject to thermal expansion and $J \times B$ acceleration, depending on the magnetic Reynolds number, and expands preferentially toward the array axis. The inward motion produces radial mass and current distributions that eventually cause the magnetic field topology to transition into a "global" configuration with open field lines around the wire cores. This results in near-steady-state, supersonic ablation streams of plasma toward the axis [43,44].

When there is not enough mass left in the wire cores, a bulk implosion phase starts that snowplows the precursor plasma. Some fraction of the array mass is left behind and does not contribute to the bulk implosion; about 40%–50% of the total mass is in the precursor plasma, 10%–30% is in the main implosion sheath, and 30%–40% is in the trailing mass [36]. The main x-ray pulse occurs as the converging snowplowed plasma compresses the precursor plasma and stagnates on axis, at which point the ion kinetic energy is thermalized and distributed to the electrons.

For the first CESZAR wire array experiments, four tungsten wires with diameter 7.5 μm and

height $h = 13$ mm were arranged on a circle with diameter $2R_a = 10$ mm. This load configuration has relatively high impedance, since a low number of very thin wires is used. An estimate of the inductance of the wire array can be calculated as [45]

$$L = \frac{\mu_0 h}{2\pi}\left[\ln\left(\frac{R_r}{R_a}\right) + \frac{1}{N}\ln\left(\frac{R_a}{NR_c}\right)\right] \approx 13 \text{ nH},$$

where $R_r = 6$ cm is the radius of the return current cage, $N = 4$ is the number of wires, and $R_c \approx 100$ μm is the radius of the coronal plasma around the wires, estimated from the literature [46].

An example of a dataset from this experiment is shown in Fig. 7. The machine charging voltage was $V_c = \pm 50$ kV. The current waveform in this configuration is quite different than the short-circuit test, with a peak current of about 380 kA and a rise time of about 200 ns, as can be seen in Fig. 7(a). The rise time allows us to calculate the load inductance as ∼14 nH, which is close to the initial estimate. Prior to the experiment, an appropriate load mass was estimated using a slug model. The 4×7.5 μm array has a linear mass of 34 μg/cm, and the model predicts implosion and stagnation at 180 ns with 380 kA peak current. Also plotted in the same figure is the signal from a 1 mm^2 Si photodiode filtered with a 10-μm-thick Al foil, used to detect x rays (the filter has a $1/e$ transmission at photon energies 1.5–1.55 and > 3.9 keV) on a radial line of sight at a distance of 0.5 m from the target. The peak in the emitted radiation can be observed around 212 ns, coincident with a small change in the shape of the load current pulse, which indicates a change in circuit impedance. This could be an indication of bulk motion of the wire plasma.

A four-frame extreme-ultraviolet (XUV) time-gated pinhole camera, consisting of a 40-mm-diameter round microchannel plate (MCP) intensifier with a gold photocathode divided into four independently triggered quadrants, was used to image the plasma. The exposure time for each frame was 5 ns, and the dashed green vertical lines in Fig. 7(a) indicate the gate start time. The diameter of the

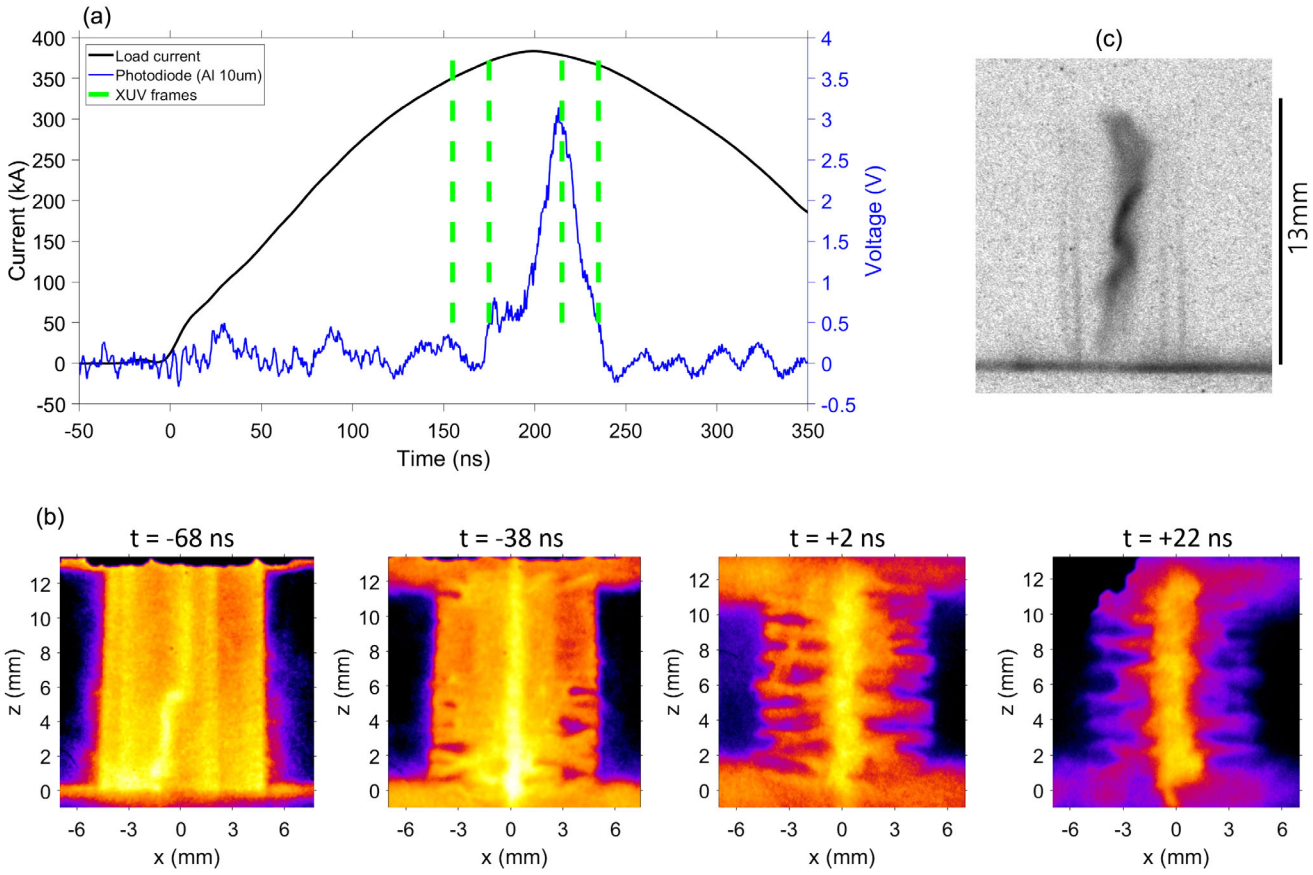

FIG. 7. Example of a wire array Z-pinch experiment on CESZAR, using 4×7.5 μm diameter wires arranged in a 10 mm circle. (a) Current pulse, x-ray photodiode signal, and XUV time-gated camera frame times. (b) Sequence of time-gated XUV pinhole images. The color scheme and contrast of the images has been enhanced for clarity. The time stamp relative to the x-ray peak emission is reported above each image. (c) Time-integrated pinhole image filtered with a 3.5 μm aluminized Mylar foil; this image comes from a different shot than (a) and (b), in order to show a precursor kink structure characteristic of a current-carrying plasma column. In all images, the anode is at the top.

pinholes was 100 μm, the image magnification was 0.5, and the spatial resolution was about 300 μm. The images were recorded on a commercial digital camera (Canon EOS Rebel T6) with a 35 mm focal length and $f/2.8$ macro lens, placed behind the MCP phosphor screen at its minimum working distance of 13 cm. Such images are shown in Fig. 7(b), with time stamps under each frame representing the start of the 5-ns gate time relative to the x-ray emission peak. The ablated plasma from the wires can be seen inside the wire circle radius. The precursor plasma stagnating on axis is also visible and, over time, accounts for a larger fraction of the emission. At later times, the bulk of the plasma implodes and develops instabilities such as the magneto-Rayleigh-Taylor (MRT) instability [47], which arises when a heavier fluid is compressed by a lighter fluid (in this case, the lighter fluid is the vacuum magnetic field). A portion of the plasma remains at larger radii as trailing mass. One possible reason for the difference in implosion and x-ray timing between the slug model and the experiment is that the precursor plasma prefills the array interior and must be compressed during the implosion, which is not modeled accurately by a simple slug model.

A time-integrated x-ray pinhole camera, using a 100-μm-diameter pinhole filtered with an aluminized Mylar foil (3.2-μm-thick Mylar coated with a 0.3-μm-thick Al layer) and a magnification of 1 was also fielded to collect images of the plasma x-ray emission ($1/e$ transmission at photon energies >1.1 keV). One example of such an image is shown in Fig. 7(c). Outlines of the wires are visible, particularly closer to the cathode electrode. The precursor plasma from wire ablation can also be seen at a radius of 1–2 mm. In the image shown, the precursor has a pronounced helical or kink structure. This was observed in a relevant fraction (but not all) of the shots and could be an indication that the precursor column is carrying some of the driver current, in agreement with similar observations made on other facilities [48–50].

For example, in Ref. [49], a kink-unstable precursor was observed when a wire-to-wire spacing of ≥ 1.6 mm was used. In our case, the wire spacing was even larger ($\sim$7 mm), which could be a cause for current advection to the precursor. In Ref. [48], precursor instability was produced when a prepulse was applied to the load before the main driver current. In our case, a prepulse can be induced through the load by pulsing the LTD cores during the active premagnetization. This prepulse can be bypassed using "passive" core premagnetization (where the cores are pulsed before installing the load) or no core premagnetization at all. This resulted in lower peak currents ($\sim$300 kA for passive premagnetization and 200–250 kA for no premagnetization), reduced or absent x-ray emission, and delayed implosions. However, time-gated XUV images showed that in these experiments the precursor can still become unstable, suggesting that the interwire spacing might be a more important factor for current advection to the precursor. Since, in general, the kink instability of the precursor column was not observed in all shots (with or without active premagnetization), a larger and more systematic dataset is required to study this phenomenon.

B. Gas puff Z pinch

The second set of experiments on the CESZAR machine were gas puff Z-pinch implosions. Gas puff Z pinches have been studied since the 1970s [51] as sources of x rays and neutrons. There are advantages and disadvantages of gas puffs relative to wire array Z pinches. The advantages of gas puffs include a better cylindrical symmetry than the discrete wires, the possibility to conduct several shots without breaking vacuum on small-scale generators which leads to a higher shot rate and larger datasets, and the possibility to tailor the density profile in a more flexible way than wires. However, this also means that the initial density profile has to be measured before the experiment, as opposed to the well-known arrangements of wires. Gas puff Z pinches are also prone to the development of the MRT instability, which is typically the dominant instability for large initial radius gas puffs, and can grow to ultimately disrupt the plasma column before maximum compression can occur [36,52].

Other disadvantages of gas puffs include the limited number of gas species (whereas there are many wire materials) that can be used. Additionally, while most wires are made of metal, the gas load is initially an electrical insulator that must undergo a phase transformation into a plasma in order to conduct the driver current.

The initial ionization can be obtained in several ways. If the driving voltage pulse exceeds the Paschen curve value [53,54], the electrons can obtain sufficient energy between successive collisions to cause an ionizing impact with a neutral atom (avalanche breakdown). If the driver has a sizable prepulse, then the prepulse may be able to produce enough ionization through the gas before the main pulse arrives. Alternatively, an external system can be used to preionize the gas before the driver pulse; several methods have been reported in the literature, including the use of microwaves [55], electron beams [56], or UV irradiation [57,58]. A uniform initial ionization is thought to improve the reproducibility and symmetry of the pinch [52].

A single, hollow argon gas shell configuration was used in the experiment on CESZAR presented here. The initial radius of the shell was $R_0 = 13$ mm with a full width at half maximum $\mathrm{FWHM}_0 = 6$ mm [59] and pinch length 13 mm. The plenum pressure in the gas injector valve was 19.3 kPa (2.8 psia), and the valve was opened 350 μs before the beginning of the driver current, producing an initial density profile with a maximum atomic number density $N_0 = (3.0 \pm 0.7) \times 10^{16}$ cm^{-3}, equivalent to a linear mass density $M/L = 9$ μg/cm.

For this experiment, no additional preionizing technique was used. However, during the core premagnetizing pulse,

a voltage is induced on the load electrodes that could cause gas ionization before the driver pulse. This hypothesis was confirmed by measuring the visible light emitted by the gas during the premagnetizing pulse alone, without energizing the LTD cavity. Light emission from the gas begins shortly after the start of the pulse and approximately follows the shape of the premagnetizing current. This is an indication of some degree of ionization in the gas. However, both this ionization and the subsequent pinch had a more inconsistent behavior at plenum pressures below 19 kPa, possibly indicating that a reliable breakdown was not occurring in the gas. We plan to study the uniformity and reproducibility of the preionization (and the subsequent implosion) due to active premagnetization and, if needed, with a dedicated preionization system in the near future.

It can be estimated [60] that, in order for several ionizing collisions to occur over a typical anode-cathode gap length of 1.5 cm and for a sufficiently high voltage ($\gtrsim$10 kV), the neutral density should be around 2×10^{16} cm^{-3}. The breakdown can already occur at a voltage much lower than the maximum (open circuit) voltage supplied by the LTD driver: the maximum cross section for electron impact ionization occurs at electron energies around 100 eV [61], which corresponds to an anode-cathode voltage of ~1 kV in the simple case of ten collisions in the A-K gap. This voltage is also quite close to the minimum of the Paschen curve. At this density, the time to develop significant ionization is a few nanoseconds. This minimum density estimate is very close to the initial conditions in our gas puff, which is a plausible explanation for unpredictable behavior at lower plenum pressure.

In addition to the XUV time-gated pinhole camera described above, a laser probing system was used for this experiment, based on a 30 ps, 20 mJ Nd:YAG laser. The laser pulse was split to produce two frames of schlieren imaging with a 20 ns interpulse delay and a single-frame 2-D Nomarski interferometer [62,63]. A knife edge was used as a beam stop for the schlieren images, and the Nomarski probe pulse was coincident in time with the first schlieren pulse. Two x-ray Si photodiodes were installed at a radial distance of 1 m from the target: a 1.0 mm^2 photodiode with a 12-μm-thick Ti filter ($1/e$ transmission at photon energies >3.7 keV) and a 0.28 mm^2 photodiode with a 10-μm-thick Al filter. The two filters have a similar transmission in the 2–4 keV spectral range, which includes the argon K-shell emission (3–4 keV), while the Al filter also has a transmission window in the 1–1.5 keV range. Neither filter allows transmission below 1 keV.

Figure 8 shows an example dataset from the gas puff *Z*-pinch experiment. The peak current was 458 kA for a charge voltage $V_c \pm 60$ kV, with a rise time of 160 ns, as seen in Fig. 8(a). The shorter rise time confirms that the gas puff load has a lower baseline inductance than the wire array.

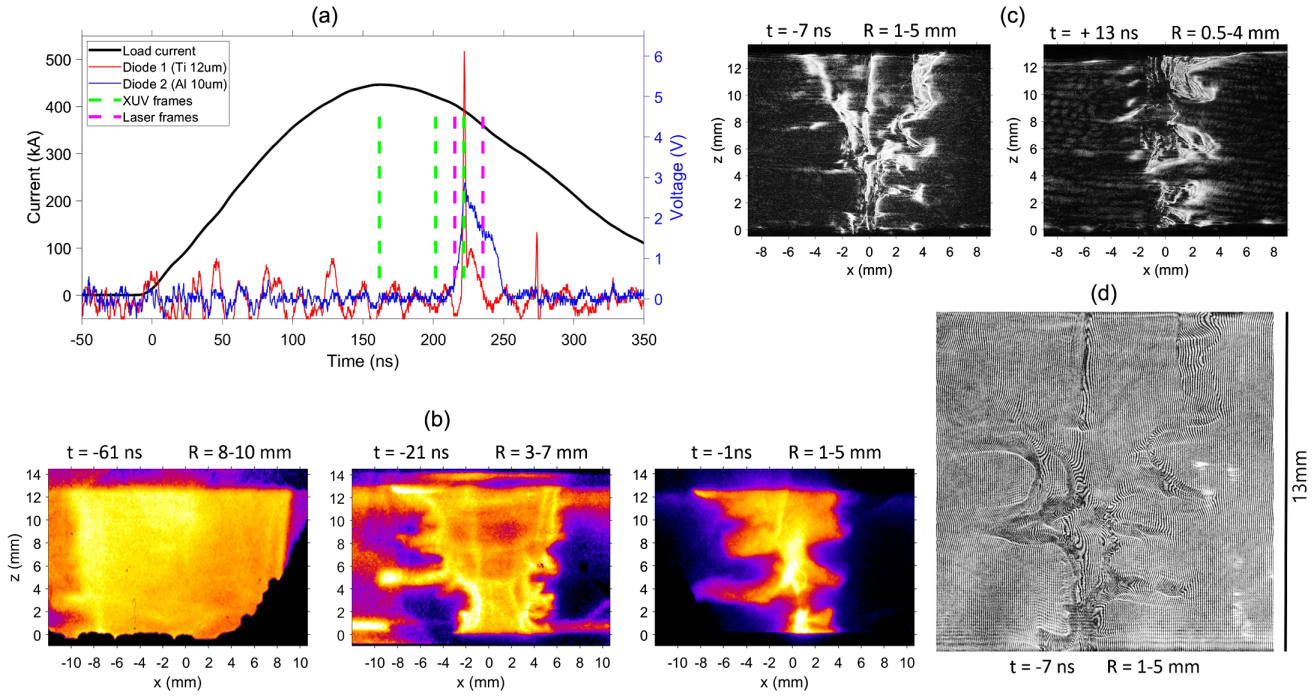

FIG. 8. Example of a gas puff *Z* pinch on CESZAR with a single, hollow Ar gas shell. (a) Current pulse, x-ray photodiode signal, timing of XUV gated camera, and laser pulses. (b) Sequence of time-gated XUV pinhole images. The color scheme and contrast of the images have been enhanced for clarity. A time stamp relative to the x-ray peak emission and an interval of values for the radius, between the leading edge of the bubbles and the trailing edge of the plasma, are reported above each image. (c) Laser schlieren images. (d) Laser Nomarski interferogram. In all the images (b)–(d), the gas injection is from the anode electrode at the top of the image.

The two photodiodes recorded emission peaks around $t = 220$ ns, marking the maximum compression. The Al-filtered photodiode registers a longer emission in the 215–250 ns time window due its transmission window at lower energy, while the Ti-filtered photodiode shows a sharp, 2-ns-wide peak centered around $t = 222$ ns.

An estimate of the implosion trajectory can be obtained by the XUV time-gated pinhole images and the laser probing images [Figs. 8(b)–8(d)]. The images are oriented with the anode electrode at the top and the cathode at the bottom, and the gas is injected from the anode side. For each image, an interval of values for the radius between the leading edge of the bubbles (minimum radius) and the trailing edge of the plasma (maximum radius) is reported. The time stamps below each image are relative to the peak of the Ti-filtered x-ray photodiode.

The average implosion velocity is 100 km/s, which is a factor of 3 lower than measured in previous experiments conducted on a 1 MA, 100 ns driver with a similar setup [64]. However, a large zippering effect and MRT instability were still observed in the plasma column, despite the slower implosion. The zippering effect is likely due to an axial density gradient in the initial gas profile, resulting in a faster implosion near the cathode side relative to the anode side. This is particularly evident from the laser interferogram [Fig. 8(d)]. In this image, the bottom end has a radius $\leq$1 mm and several broken fringes, indicating a plasma density $\geq 2 \times 10^{18}$ cm^{-3}; on the other hand, the top end of the pinch has a radius of $\approx$5 mm, with uninterrupted fringes and a phase shift corresponding to an electron density of $\approx 7 \times 10^{17}$ cm^{-3}. The zippering effect can be mitigated in a few ways, for example, allowing for a longer gas flow time before the start of the driver pulse, in order to reduce the axial gradients associated with transient gas flow, or using a nozzle with a higher Mach number, resulting in a more collimated gas flow.

The MRT instability, characterized by radial fingerlike structures, is related to the implosion acceleration and is particularly evident in these single-shell implosions. Because of zippering and MRT instability growth, the plasma column disrupts first near the cathode electrode, coincident in time with the K-shell x-ray emission peak (Ti-filtered photodiode). Mitigation of MRT instability growth has received significant attention in the literature, and several techniques have been investigated to reduce the impact of MRT instability on Z pinches, including sheared flow [65], field-line tension via addition of an external axial magnetic field B_z [66,67], and tailored or multishell density profiles [58,68–70].

We plan to introduce and study mitigation techniques in future experiments on this machine. Nevertheless, these gas puff Z-pinch experiments are a relevant initial result from the operation of the CESZAR machine.

The implosion trajectory was compared to 1D magnetohydrodynamic (MHD) simulations conducted with the resistive-MHD code TRAC-II [71]. Figure 9 shows a comparison of the measured and simulated current pulse (where the simulation circuit parameters are the same as discussed in Sec. III). The two waveforms agree until ~20 ns prior to stagnation, where the 1D simulation has a more pronounced inductive notch. The measured x-ray emission time is within 3 ns of the stagnation time in the simulation. However, the 1D simulation does not account for zippering or MRT instability and overestimates the plasma compression when compared to 2D or 3D problems. This is consistent with the comparison in implosion trajectory: The simulated plasma radius (red solid line in Fig. 9) shows larger deviations in the last phase of compression, when compared to the average radius or to the minimum radius [e.g., near the cathode in Fig. 8(b)] from experimental images. The stagnation radius is 0.3 mm in the simulation, which is ~8× smaller than the average radius and ~3× smaller than the minimum radius from the last of the XUV images. However, this does not necessarily mean that a smaller plasma radius is not reached in the experiment at times different than the acquired images or on a timescale shorter than the XUV camera 5 ns gate time; the leading edge of the leading bubble could, in principle, have an equal or higher convergence than 1D simulations. However, if the current was flowing in a plasma with a radius of $\leq$2 mm, as shown by the XUV images, the load inductance would spike to $\geq$9 nH in the final implosion phase, which should result in a pronounced inductive notch. The absence of a large dip in the measured waveform indicates that the current could instead be shunted at larger radii.

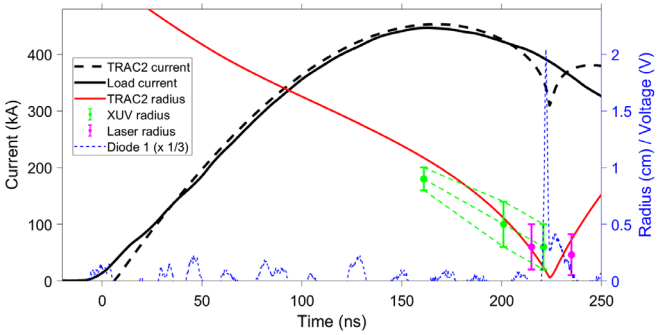

FIG. 9. Comparison of gas puff implosion with results from a 1D simulation using the TRAC-II MHD code: driver current, implosion radius, and x-ray emission. The dashed green lines represent the trajectory of the plasma leading edge (bubbles), average radius, and trailing edge (spikes).

In principle, it should also be expected that at least the leading edge of the instability has a higher implosion velocity than 1D simulations. The TRAC-II simulation calculates an average velocity of 110 km/s over the entire implosion, which is in good agreement with the measured value. However, the peak implosion velocity in the simulation is 300 km/s: The maximum velocity is reached close

to stagnation, when in the experiment instabilities increase the velocity spread and cause a less accurate measurement. The green dashed lines in Fig. 9 represent the implosion trajectories of the leading edge, average value, and trailing edge of the plasma radius. The leading edge has an implosion velocity slightly smaller than the simulation, while the trailing edge is substantially slower. This could also be an indication that current is flowing at a larger radius. Future experiments will investigate these implosion features in more detail.

For a final plasma radius of 1 mm, the vacuum magnetic field energy is 1.1 kJ, or about 26% of the capacitor stored energy. This provides a constraint on how much energy is coupled to the load itself. If we assume that the entire mass of the gas puff is swept up during the implosion and is accelerated to the average implosion velocity 100 km/s, we can estimate the mean kinetic energy imparted by the driver to be $E_{\mathrm{K}}^{(\mathrm{m})} = 60$ J. The 1D simulation results have a larger deviation from the experiment near stagnation, but that is also when the vacuum $J \times B$ force and plasma kinetic energy are largest. An estimate of the implosion kinetic energy to be compared to the experiment can be calculated when the plasma radius reaches 1 mm in the simulation: in this case, we find $E_{\mathrm{K}}^{(\mathrm{s})} = 380$ J. While $E_{\mathrm{K}}^{(\mathrm{m})}$ is an underestimation of the maximum kinetic energy since it relies on an average velocity, $E_{\mathrm{K}}^{(\mathrm{s})}$ is likely an overestimation due to the higher convergence and higher plasma velocity. The 6× discrepancy in kinetic energy between the simulation and experiment can be explained by a 2.5× difference in implosion velocity, i.e., 100 km/s in the experiment versus 250 km/s in the simulation. With these constraints, we can say that the conversion efficiency to kinetic energy in the load is between 2% and 9% in these preliminary gas puff Z-pinch experiments.

We plan to perform more comprehensive measurements of energy coupled to the plasma in future experiments, as well as experiments to improve the energy coupling. Higher-energy coupling can be achieved by using a lower total mass in the gas puff, after installing a gas preionization system, and adopting some of the above-mentioned measures to improve the pinch stability. Preliminary simulations with improved load setups indicate that over 20% of the stored energy can be transferred to a gas puff load.

V. CONCLUSIONS

The low-impedance linear transformer driver CESZAR was commissioned and tested at UC San Diego. Its nominal parameters are 0.9 MA peak current into a short-circuit load at ±100 kV charge voltage, 170 ns quarter period, and 0.18 Ω impedance.

At present, CESZAR can operate at a charge voltage $V_{\mathrm{c}} \pm 60$ kV, producing peak currents in the range of 400–500 kA with a 160–200 ns quarter period, depending on the load impedance. Operation at higher voltages will be achieved in the near future. Short-circuit tests done at $V_{\mathrm{c}} \pm 60$ kV show a slightly higher inductance than the circuit model and a comparable peak current (scaled for charge voltage).

Two sets of experiments have been performed on the machine at this reduced current level, one with a W wire array Z-pinch load and one with a hollow-shell Ar gas puff Z-pinch load. The preliminary data are consistent with literature findings and show that these kinds of experiments can successfully be conducted on a low-impedance LTD, but the current pulse amplitude and rise time depend on the load impedance. The dynamics of the gas puff Z pinch were consistent with results from 1D MHD simulations, with the caveat that zippering and MRT instabilities, not captured by the simulation, played a large role in the experiment near stagnation.

The CESZAR machine will be used primarily for low-inductance experiments investigating fundamental properties of Z pinches: the study of instability mitigation techniques in the imploding plasma, the distribution of magnetic fields in single-shell and multishell implosions with or without an external axial magnetic field, and the dynamics of different species in multispecies interfaces. Additionally, high shot-count experiments on CESZAR will help train young scientists in pulsed power plasma experiments, develop diagnostic techniques, and understand how efficiently the driver energy from a compact, low-impedance LTD can be coupled to plasma loads.

ACKNOWLEDGMENTS

This work was supported by the Department of Defense, Air Force Office of Scientific Research under Grant No. FS9550-18-1-0384 and by the Department of Energy, National Nuclear Security Administration under Grant No. DE-NA0003842. We thank Sandia National Laboratories for the donation of the LTD-III cavity.

[1] M. G. Mazarakis *et al.*, High current, 0.5-MA, fast, 100-ns, linear transformer driver experiments, Phys. Rev. ST Accel. Beams **12**, 050401 (2009).

[2] A. A. Kim *et al.*, Development and tests of fast 1-MA linear transformer driver stages, Phys. Rev. Accel. Beams **12**, 050402 (2009).

[3] W. A. Stygar, M. E. Cuneo, D. I. Headley, H. C. Ives, R. J. Leeper, M. G. Mazarakis, C. L. Olson, J. L. Porter, T. C. Wagoner, and J. R. Woodworth, Architecture of petawatt-class z-pinch accelerators, Phys. Rev. Accel. Beams **10**, 030401 (2007).

[4] W. A. Stygar *et al.*, Shaping the output pulse of a linear-transformer-driver module, Phys. Rev. Accel. Beams **12**, 030402 (2009).

[5] A. A. Kim, M. G. Mazarakis, V. A. Sinebryukhov, S. N. Volkov, S. S. Kondratiev, V. M. Alexeenko, F. Bayol,

G. Demol, and W. A. Stygar, Square pulse linear transformer driver, Phys. Rev. Accel. Beams **15**, 040401 (2012).
[6] B. M. Kovalchuk, A. V. Kharlov, E. V. Kumpyak, and A. A. Zherlitsyn, Pulse generators based on air-insulated linear-transformer-driver stages, Phys. Rev. Accel. Beams **16**, 050401 (2013).
[7] B. M. Koval'chuk, V. A. Vizir', A. A. Kim, E. V. Kumpyak, S. V. Loginov, A. N. Bastrikov, V. V. Chervyakov, N. V. Tsoi, P. Monjaux, and D. Kh'yui, Fast primary storage device utilizing a linear pulse transformer, Russ. Phys. J. **40**, 1142 (1997).
[8] W. A. Stygar *et al.*, Conceptual designs of two petawatt-class pulsed-power accelerators for high-energy-density-physics experiments, Phys. Rev. Accel. Beams **18**, 110401 (2015).
[9] R. D. McBride *et al.*, A Primer on Pulsed Power and Linear Transformer Drivers for High Energy Density Physics Applications, IEEE Trans. Plasma Sci. **46**, 3928 (2018).
[10] R. Spielman, D. Froula, G. Brent, E. Campbell, D. Reisman, M. Savage, M. Shoup, W. Stygar, and M. Wisher, Conceptual design of a 15-TW pulsed-power accelerator for high-energy-densityâ physics experiments, Matter Radiat. Extremes **2**, 204 (2017).
[11] W. Jiang, Review of solid-state linear transformer driver technology, Matter Radiat. Extremes **3**, 159 (2018).
[12] A. A. Kim and M. G. Mazarakis, The Story of the LTD Development, IEEE Trans. Plasma Sci. **48**, 749 (2020).
[13] R. M. Gilgenbach *et al.*, MAIZE: A 1 MA LTD-Driven Z-Pinch at The University of Michigan, AIP Conf. Proc. **1088**, 259 (2009).
[14] S. C. Bott *et al.*, 250 kA compact linear transformer driver for wire array z-pinch loads, Phys. Rev. Accel. Beams **14**, 050401 (2011).
[15] P. A. Gourdain, M. Evans, B. Foy, D. Mager, R. McBride, and R. Spielman, HADES: A high amperage driver for extreme states, arXiv:1705.04411.
[16] J. D. Douglass *et al.*, 100 GW linear transformer driver cavity: Design, simulations, and performance, Phys. Rev. Accel. Beams **21**, 120401 (2018).
[17] R. Maisonny, M. Ribière, M. Toury, J. M. Plewa, M. Caron, G. Auriel, and T. d'Almeida, Investigating the performances of a 1 MV high pulsed power linear transformer driver: from beam dynamics to x radiation, Phys. Rev. Accel. Beams **19**, 120401 (2016).
[18] D. Yanuka, S. Theocharous, and S. N. Bland, Pulsed power driven cylindrical wire array explosions in different media, Phys. Plasmas **26**, 122704 (2019).
[19] A. A. Kim, B. M. Kovalchuk, E. V. Kumpjak, and N. V. Zoi, 0.75 MA, 400 ns rise time LTD stage, in *Digest of Technical Papers. Proceedings of the 12th IEEE International Pulsed Power Conference (Cat. No. 99CH36358)* (IEEE, New York, 1999), Vol. 2, pp. 955–958.
[20] A. Kim, B. Kovalchuk, V. Kokshenev, A. Shishlov, N. Ratakhin, V. Oreshkin, V. Rostov, V. Koshelev, and V. Losev, Review of high-power pulsed systems at the Institute of High Current Electronics, Matter Radiat. Extremes **1**, 201 (2016).
[21] L. Zhou, Z. Li, Z. Wang, C. Liang, M. Li, J. Qi, and Y. Chu, Design of a 5-MA 100-ns linear-transformer-driver accelerator for wire array Z-pinch experiments, Phys. Rev. Accel. Beams **19**, 030401 (2016).
[22] L. Chen *et al.*, Development of a fusion-oriented pulsed power module, Phys. Rev. Accel. Beams **22**, 030401 (2019).
[23] J. R. Woodworth *et al.*, Compact 810 kA linear transformer driver cavity, Phys. Rev. Accel. Beams **14**, 040401 (2011).
[24] J. R. Woodworth, W. A. Stygar, L. F. Bennett, M. G. Mazarakis, H. D. Anderson, M. J. Harden, J. R. Blickem, F. R. Gruner, and R. White, New low inductance gas switches for linear transformer drivers, Phys. Rev. Accel. Beams **13**, 080401 (2010).
[25] A. P. Shah, P. C. Campbell, S. M. Miller, J. M. Woolstrum, B. J. Sporer, S. G. Patel, N. M. Jordan, R. M. Gilgenbach, and R. D. McBride, Optimization of switch diagnostics on the MAIZE linear transformer driver, Rev. Sci. Instrum. **90**, 124707 (2019).
[26] E. M. Waisman, D. B. Reisman, B. S. Stoltzfus, W. A. Stygar, M. E. Cuneo, T. A. Haill, J.-P. Davis, J. L. Brown, C. T. Seagle, and R. B. Spielman, Optimization of current waveform tailoring for magnetically driven isentropic compression experiments, Rev. Sci. Instrum. **87**, 063906 (2016).
[27] A. M. Steiner, D. A. Yager-Elorriaga, S. G. Patel, N. M. Jordan, R. M. Gilgenbach, A. S. Safronova, V. L. Kantsyrev, V. V. Shlyaptseva, I. Shrestha, and M. T. Schmidt-Petersen, Determination of plasma pinch time and effective current radius of double planar wire array implosions from current measurements on a 1-MA linear transformer driver, Phys. Plasmas **23**, 101206 (2016).
[28] O. A. Hurricane, Optimized minimal inductance transmission line configuration for Z-pinch experiments, J. Appl. Phys. **95**, 4503 (2004).
[29] P. C. Campbell, J. M. Woolstrum, F. Antoulinakis, T. M. Jones, D. A. Yager-Elorriaga, S. M. Miller, N. M. Jordan, Y. Y. Lau, R. M. Gilgenbach, and R. D. Mcbride, Diagnostic and power feed upgrades to the MAIZE facility, IEEE Trans. Plasma Sci. **46**, 3973 (2018).
[30] R. V. Shapovalov and R. B. Spielman, Radial vacuum power-flow feed for LTD-III cavity for X-pinch and Z-pinch experiments, technical report for Sandia National Laboratories, Idaho State University, Pocatello, ID, 2016.
[31] M. L. Kiefer and M. M. Widner, SCREAMER–A single-line pulsed-power design tool, in *Proceedings of the 5th IEEE Pulsed Power Conference* (IEEE, New York, 1985), p. 685.
[32] R. B. Spielman and Y. Gryazin, SCREAMER V4.0–A powerful circuit analysis code, in *Proceedings of the 20th IEEE Pulsed Power Conference* (IEEE, New York, 2015), pp. 1–6.
[33] R. B. Spielman and D. B. Reisman, On the design of magnetically insulated transmission lines for z-pinch loads, Matter Radiat. Extremes **4**, 027402 (2019).
[34] C. Stallings, K. Nielsen, and R. Schneider, Multiple-wire array load for high-power pulsed generators, Appl. Phys. Lett. **29**, 404 (1976).
[35] R. B. Spielman *et al.*, Tungsten wire-array Z-pinch experiments at 200 TW and 2 MJ, Phys. Plasmas **5**, 2105 (1998).

[36] M. G. Haines, A review of the dense Z-pinch, Plasma Phys. Controlled Fusion **53**, 093001 (2011).

[37] M. C. Jones *et al.*, X-ray power and yield measurements at the refurbished Z machine, Rev. Sci. Instrum. **85**, 083501 (2014).

[38] S. V. Lebedev *et al.*, Physics of wire array Z-pinch implosions: Experiments at Imperial College, Plasma Phys. Controlled Fusion **47**, A91 (2005).

[39] S. V. Lebedev, R. Aliaga-Rossel, S. N. Bland, J. P. Chittenden, A. E. Dangor, M. G. Haines, and I. H. Mitchell, The dynamics of wire array Z-pinch implosions, Phys. Plasmas **6**, 2016 (1999).

[40] S. Lebedev, D. Ampleford, S. Bland, S. Bott, J. Chittenden, C. Jennings, M. Haines, J. Palmer, and J. Rapley, Implosion dynamics of wire array Z-pinches: Experiments at Imperial College, Nucl. Fusion **44**, S215 (2004).

[41] S. V. Lebedev, F. N. Beg, S. N. Bland, J. P. Chittenden, A. E. Dangor, M. G. Haines, K. H. Kwek, S. A. Pikuz, and T. A. Shelkovenko, Effect of discrete wires on the implosion dynamics of wire array Z pinches, Phys. Plasmas **8**, 3734 (2001).

[42] T. W. L. Sanford *et al.*, Improved Symmetry Greatly Increases X-Ray Power from Wire-Array *Z*-Pinches, Phys. Rev. Lett. **77**, 5063 (1996).

[43] J. Greenly, M. Martin, I. Blesener, D. Chalenski, P. Knapp, and R. McBride, The role of flux advection in the development of the ablation streams and precursors of wire array Z-pinches, AIP Conf. Proc. **1088**, 53 (2009).

[44] M. R. Martin, C. E. Seyler, and J. B. Greenly, The role of magnetic field in the transition to streaming ablation in wire arrays, Phys. Plasmas **17**, 052706 (2010).

[45] E. V. Grabovski, G. G. Zukakishvili, K. N. Mitrofanov, G. M. Olenik, I. N. Frolov, and P. V. Sasorov, Study of the magnetic fields and soft X-ray emission generated in the implosion of double wire arrays, Plasma Phys. Rep. **32**, 32 (2006).

[46] T. A. Shelkovenko, S. A. Pikuz, J. D. Douglass, I. C. Blesener, J. B. Greenly, R. D. McBride, D. A. Hammer, and B. R. Kusse, Wire core and coronal plasma expansion in wire-array Z pinches with small numbers of wires, Phys. Plasmas **14**, 102702 (2007).

[47] E. G. Harris, Rayleigh-Taylor instabilities of a collapsing cylindrical shell in a magnetic field, Phys. Fluids **5**, 1057 (1962).

[48] F. N. Beg, S. V. Lebedev, S. N. Bland, J. P. Chittenden, A. E. Dangor, and M. G. Haines, The effect of current prepulse on wire array Z-pinch implosions, Phys. Plasmas **9**, 375 (2002).

[49] R. D. McBride *et al.*, Implosion dynamics and radiation characteristics of wire-array Z pinches on the Cornell Beam Research Accelerator, Phys. Plasmas **16**, 012706 (2009).

[50] V. V. Ivanov, J. P. Chittenden, S. D. Altemara, N. Niasse, P. Hakel, R. C. Mancini, D. Papp, and A. A. Anderson, Study of the Internal Structure and Small-Scale Instabilities in the Dense *Z* Pinch, Phys. Rev. Lett. **107**, 165002 (2011).

[51] J. Shiloh, A. Fisher, and N. Rostoker, *Z* Pinch of a Gas Jet, Phys. Rev. Lett. **40**, 515 (1978).

[52] J. L. Giuliani and R. J. Commisso, A review of the gas-puff Z-Pinch as an X-ray and neutron source, IEEE Trans. Plasma Sci. **43**, 2385 (2015).

[53] F. Paschen, Ueber die zum Funkenübergang in Luft, Wasserstoff und Kohlensäure bei verschiedenen Drucken erforderliche Potentialdifferenz, Ann. Phys. (Berlin) **273**, 69 (1889).

[54] M. A. Lieberman and A. J. Lichtenberg, *Principles of Plasma Discharges and Materials Processing* (Wiley, Hoboken, NJ, 2005), Chap. 14.3.

[55] C. Stallings, K. Childers, I. Roth, and R. Schneider, Imploding argon plasma experiments, Appl. Phys. Lett. **35**, 524 (1979).

[56] E. Ruden, H. U. Rahman, A. Fisher, and N. Rostoker, Stability enhancement of a low initial density hollow gasâ puff z pinch by e-beam preionization, J. Appl. Phys. **61**, 1311 (1987).

[57] B. Moosman, B. V. Weber, S. J. Stephanakis, R. J. Commisso, and A. Fisher, Measurements of gas preionization for plasma radiation sources, Rev. Sci. Instrum. **70**, 672 (1999).

[58] N. Qi *et al.*, Study of gas-puff Z-pinches on COBRA, Phys. Plasmas **21**, 112702 (2014).

[59] F. Conti, J. C. Valenzuela, N. Aybar, F. J. Wessel, M. P. Ross, J. Narkis, H. U. Rahman, E. Ruskov, and F. N. Beg, Characterization of a liner-on-target gas injector for staged Z-pinch experiments, IEEE Trans. Plasma Sci. **46**, 3855 (2018).

[60] D. D. Ryutov, M. S. Derzon, and M. K. Matzen, The physics of fast *Z* pinches, Rev. Mod. Phys. **72**, 167 (2000).

[61] P. L. Bartlett and A. T. Stelbovics, Calculation of electron-impact total-ionization cross sections, Phys. Rev. A **66**, 012707 (2002).

[62] R. Benattar, C. Popovics, and R. Sigel, Polarized light interferometer for laser fusion studies, Rev. Sci. Instrum. **50**, 1583 (1979).

[63] J. Ruiz-Camacho, F. N. Beg, and P. Lee, Comparison of sensitivities of Moiré deflectometry and interferometry to measure electron densities inz-pinch plasmas, J. Phys. D **40**, 2026 (2007).

[64] F. Conti, N. Aybar, J. Narkis, J. C. Valenzuela, H. U. Rahman, E. Ruskov, E. Dutra, S. Haque, A. Covington, and F. N. Beg, Study of stability in a liner-on-target gas puff Z-pinch as a function of pre-embedded axial magnetic field, Phys. Plasmas **27**, 012702 (2020).

[65] U. Shumlak, R. P. Golingo, B. A. Nelson, and D. J. D. Hartog, Evidence of Stabilization in the Z-Pinch, Phys. Rev. Lett. **87**, 205005 (2001).

[66] M. R. Weis, P. Zhang, Y. Y. Lau, I. M. Rittersdorf, J. C. Zier, R. M. Gilgenbach, M. H. Hess, and K. J. Peterson, Temporal evolution of surface ripples on a finite plasma slab subject to the magneto-Rayleigh-Taylor instability, Phys. Plasmas **21**, 122708 (2014).

[67] M. R. Weis, P. Zhang, Y. Y. Lau, P. F. Schmit, K. J. Peterson, M. Hess, and R. M. Gilgenbach, Coupling of sausage, kink, and magneto-Rayleigh-Taylor instabilities in a cylindrical liner, Phys. Plasmas **22**, 032706 (2015).

[68] A. L. Velikovich, F. L. Cochran, and J. Davis, Suppression of Rayleigh-Taylor Instability in *Z*-Pinch Loads with Tailored Density Profiles, Phys. Rev. Lett. **77**, 853 (1996).

[69] H. Sze, J. S. Levine, J. Banister, B. H. Failor, N. Qi, P. Steen, A. L. Velikovich, J. Davis, and A. Wilson, Magnetic Rayleigh-Taylor instability mitigation and efficient radiation production in gas puff Z-pinch implosions, Phys. Plasmas **14**, 056307 (2007).

[70] A. G. Rousskikh, A. S. Zhigalin, V. I. Oreshkin, V. Frolova, A. L. Velikovich, G. Y. Yushkov, and R. B. Baksht, Effect of the axial magnetic field on a metallic gas-puff pinch implosion, Phys. Plasmas **23**, 063502 (2016).

[71] D. B. Reisman, Numerical simulation of fiber and wire array Z-pinches with Trac-II, Ph.D. thesis, University of California, Davis, 1998, Lawrence Livermore National Laboratory Report No. UCRL-LR-131742.